Investigation of Wave Power Conversion Efficiency and Hydrodynamic Characteristics of a Floating Twin-Hybrid Wave-Energy Device in Random Waves

Nourah Almashan[1]; Subramaniam Neelamani[2]; Benhur Joseph Raju[3]; and Dana Al-Houti[4]

Abstract: The potential advantages of wave-energy converters can be extended beyond their capability to produce clean and safe energy, including wave attenuation using hybrid devices. This study presents an experimental investigation of the power production and wave attenuation capabilities of a floating twin-raft hybrid device. Model tests were performed using different random waves and damping values for a simulated power take-off (PTO) system. The coefficients of wave transmission (K_t), reflection (K_r), dissipation (K_l), and mechanical power conversion efficiencies for the seaside raft (η_1) and rear side raft (η_2) were estimated. It was observed that varying the peak wave period considerably affects the hydrodynamic characteristics, whereas wave height has a lesser influence. The PTO simulation is an area of uncertainty in wave-energy converters. Moreover, the study of the influence of PTO damping on device performance is new. Varying the PTO damping marginally influenced the K_t, K_r, and K_l, whereas the power conversion efficiencies of both seaside and rear-side rafts varied significantly. η_1 and η_2 were maximized at low-input wave height conditions. As the wave height increased, η_1 and η_2 decreased. This occurred due to the significant wave-energy dissipation. Liberal ($K_t < 0.5$ and η_1 or $\eta_2 > 0.2$) and stringent ($K_t < 0.2$ and η_1 or $\eta_2 > 0.4$) hydrodynamic performance conditions were used to discuss the effective range of available wave frequencies under different PTO damping conditions. This would help identify the areas where this type of device can be applied. This study validated the concept of a floating twin-body hybrid wave-energy converter. This study belongs to the concept development stage of wave-energy conversion technologies, and the conclusions can help further develop and improve this concept. **DOI: 10.1061/JWPED5.WWENG-2162**.

Author keywords: Hybrid wave-energy converter; Twin-floating breakwater; Mechanical energy; Energy conversion efficiency; Wave transmission; Reflection; Dissipation.

Introduction

The theoretical total potential of wave-energy resources worldwide is approximately 29,500 TWh/year (Mørk et al. 2010). If utilized extensively, it may contribute significantly to the electrical energy supply of many coastal countries (Barstow et al. 2008). In 1799, the first patent was filed for a wave-energy converter (WEC) (Clément et al. 2002). The first floating wave-energy device was developed by Masuda (1986) in Japan for use in powering navigation buoys. Since then, many scientists worldwide have been working on different aspects of WECs. This has resulted in several hundred patents in the 20th century (McCormick 1981; Pelc and Fujita 2002; Falnes 2007). Wave energy has the second-largest potential among all ocean renewable energy resources. This has motivated the development of more technologies (Ilyas et al. 2014).

Globally, scientists have predominantly worked on three main concepts of wave-energy conversion technologies: point absorbers, oscillating water columns (OWCs), and overtopping devices. Over the last decade, many researchers have started working on hybrid concepts to achieve better cost–benefits (Zhao et al. 2019). Hybrid systems have been developed for various applications. For example, hybrid floating breakwaters can be used to aerate aquaculture cages by converting wave energy into pressurized air to improve water quality. Extracting energy from the dynamic response of a floating breakwater can aid in power generation and reduce wave transmission. Certain recent potential studies related to the performance and other technical aspects of hybrid floating breakwaters are summarized in the following.

The experimental studies on hybrid breakwaters include those on devices such as rectangular floating breakwaters with and without pneumatic chambers (He et al. 2012), pile-supported OWC structures (He and Huang 2014), and rectangular floating breakwaters with dual pneumatic chambers (He et al. 2017). Martinelli et al. (2016) experimentally studied the hydrodynamic performance and wave-energy conversion characteristics of a hybrid structure by combining a WEC, ShoWED, and a floating breakwater. The reflection and transmission characteristics of the hybrid structures were evaluated, and the advantages of the hybrid floating breakwater were compared with those of a conventional floating breakwater. This was particularly effective for long waves. Ning et al. (2016) experimentally investigated the hydrodynamic performance of a pile-restrained WEC-type floating breakwater. This hybrid

---

[1] Associate Professor, Dept. of Civil Engineering, Kuwait Univ., P.O. Box 5969, Safat 13060, Kuwait (corresponding author). ORCID: https://orcid.org/0000-0002-4627-5195. Email: nourah.almashan@ku.edu.kw

[2] Senior Research Scientist, Kuwait Institute for Scientific Research, Coastal Management Program, P.O. Box 24885, Safat 13109, Kuwait. Email: nsubram@kisr.edu.kw

[3] Research Assistant, Dept. of Civil Engineering, Kuwait Univ., P.O. Box 5969, Safat 13060, Kuwait. Email: josephbenhur8@gmail.com

[4] Research Associate, Kuwait Institute for Scientific Research, Coastal Management Program, Kuwait. ORCID: https://orcid.org/0000-0002-6317-5946. Email: dhouti@kisr.edu.kw

Note. This manuscript was submitted on May 8, 2024; approved on October 4, 2024; published online on November 26, 2024. Discussion period open until April 26, 2025; separate discussions must be submitted for individual papers. This paper is part of the ***Journal of Waterway, Port, Coastal, and Ocean Engineering***, © ASCE, ISSN 0733-950X.

J. Waterway, Port, Coastal, Ocean Eng., 2025, 151(2): 04024025

system integrates an oscillating buoy WEC with a vertical pile-restrained floating breakwater. They investigated the effects of parameters such as the wave period, wave height, system dimensions, and excitation current on the hydrodynamic performance of the hybrid device. The results indicated that the power take-off damping force, draft, and relative width between the floating breakwater and wavelength substantially influenced the hydrodynamic performance of the system. Ning et al. (2017) analytically investigated the hydrodynamic performance of a dual-pontoon WEC breakwater. The pontoons were constrained to undergo only heave motion.

The effects of geometrical parameters on hydrodynamic properties, such as wave reflection, transmission, and efficiency, were studied. The natural frequency of the heave motion and the spacing of two pontoons were observed to be critical factors affecting the performance of the integrated system. A comparison between the results of dual- and single-pontoon breakwaters revealed that the effective frequency range of the dual-pontoon system was broader than that of the single-pontoon system with an equal total volume. This study demonstrated that using twin pontoons is better than using single pontoons in terms of wave attenuation and power conversion efficiency enhancement. Ning et al. (2018) proposed that the cost of WECs could be reduced significantly by integrating them into other marine facilities, particularly in areas with mild wave climates. To reduce the cost and increase efficiency, a hybrid WEC system was proposed. It comprises a linear array of oscillating buoy-type WECs attached to the weather side of a fixed-type floating pontoon as the base structure. Zheng and Zhang (2018) conducted a detailed analytical study on wave power extraction from a hybrid WEC consisting of an OWC device and a float at the seaside. The study revealed that the power-extraction capacity could be improved for a broad range of wave conditions by combining an isolated OWC and an isolated float. Zhang et al. (2019) numerically investigated the hydrodynamic performance of floating-box-type and Berkeley-wedge-type WEC devices. The Berkeley-wedge-type WEC device was observed to have a better power conversion efficiency than the floating box-type breakwater. Zhao et al. (2019) reviewed various hybrid floating wave-energy-type breakwaters. Although many WEC concepts are available, the authors revealed that high construction costs hinder engineering applications and commercialization. Construction costs can be reduced by combining different structures into an integrated system, which enables cost-sharing, space-sharing, and multifunctionality.

Different approaches to integrating floating breakwaters and WECs are summarized in this review. Cabral et al. (2020) investigated the performance of a hybrid WEC integrated into a harbor breakwater. This system comprised an OWC and an overtopping device integrated into a rubble mound breakwater. Hybridization can yield systems with higher efficiencies than their components for a broader range of wave climates. Peng et al. (2020) experimentally investigated the hydrodynamic performance of a hybrid system that combines a fixed breakwater and an oscillating buoy-type WEC. An energy converter was designed to extract wave power using the wave-induced heave motions of three floating pontoons in front of a fixed breakwater. A proof-of-concept study on multiple OWC WECs integrated into a floating breakwater was conducted by Howe et al. (2020). It revealed a maximum energy capture efficiency of 80%. Peng et al. (2021) assessed the performance of the wave-energy device of a triple pontoon-type floating hybrid based on laboratory experiments. They observed that the power-conversion efficiency was higher when all three pontoons had identical drafts. Zhang et al. (2023) conducted studies to optimize a three-dimensional hybrid system combining a floating breakwater and a WEC array. The study guided the design and optimization of hybrid WEC–breakwater systems for practical engineering applications. These studies identified that hybrid systems offer better wave attenuation and energy conversion than standalone systems, and combining multiple concepts can broaden the range of effective wave-capture conditions. Hybrid concepts could potentially reduce construction costs through shared infrastructure and multifunctionality.

Cheng et al. (2022) conducted a numerical and experimental investigation of two types of floating breakwater-integrated WECs: a single-pontoon oscillating body and a double-pontoon oscillating column breakwater. The energy conversion and attenuation properties of the OWC breakwater were determined to be better than those of the single pontoon oscillating body. Shahabi-Nejad and Nikseresht (2022) comprehensively investigated a hybrid WEC (including an OWC and a horizontal floating cylinder) based on numerical simulations using the ANSYS-Fluent software program. It was demonstrated that the efficiency of the hybrid WEC is higher than that of a single OWC and a single horizontal floating cylinder. Rosa-Santos et al. (2022) revealed the advantages of hybrid systems for harvesting marine energy. The importance of research to address challenges such as survivability, resilience, and reliability during the installation of WEC has been emphasized. Li et al. (2023) discussed the novel concept of a floating two-body WEC excited by heave motion. A numerical investigation of point absorber-integrated breakwater using computational fluid dynamics was performed by Yang et al. (2023). They focused on the influence of the distance between the breakwater and the point absorber. The numerical model was validated using publicly available experimental data from the study of waveguide point absorbers reported by Ransley et al. (2017). In addition to the challenges of developing cost-effective technologies (affordability), marine renewable energy (MRE) encounters key issues in contributing to decarbonization (sustainability), intermittent characteristics (reliability), and location/marine environmental constraints (resilience). Hybridization helps mitigate the excessive production costs and intermittent characteristics of MRE.

This literature review revealed that many noteworthy studies have been conducted on different types of hybrid-WEC floating breakwaters worldwide that have demonstrated that hybrid WEC systems are better in terms of economics and overall performance. However, few studies have reported the mechanical power absorption characteristics and hydrodynamic performance (wave transmission, reflection, and dissipation characteristics) of twin-raft hybrid WEC devices. A hybrid floating WEC excited by the pitch motion of floating bodies was considered in this study. This WEC consists of two floating pontoon structures maintained at a certain distance from the center of gravity. These are connected to a spatially fixed circular shaft using steel arms. Hence, when a wave acts on these pontoons or rafts, they can swing freely on the shaft. The resistance provided by the power take-off (PTO) system is an important parameter. It is simulated by attaching steel wires to the turning shaft and adding known weights at the end of the wire. This wire is passed through a frictionless pulley to provide resistance or damping to the swinging shaft (PTO damping). When the pontoon responds during the wave interaction, the force on the wire varies owing to acceleration and deceleration, and the linear velocity of the wire along its axial direction varies. Measuring the variation in force and displacement of the wire helps assess the mechanical power provided by the dynamically responding floating pontoon. More details are provided in the “Methodology” section.

The main objective of this study was to model physically a floating twin-raft WEC that also functions as a floating breakwater and analyze the mechanical power conversion efficiency of the rafts (while interacting with waves), wave transmission, reflection, and

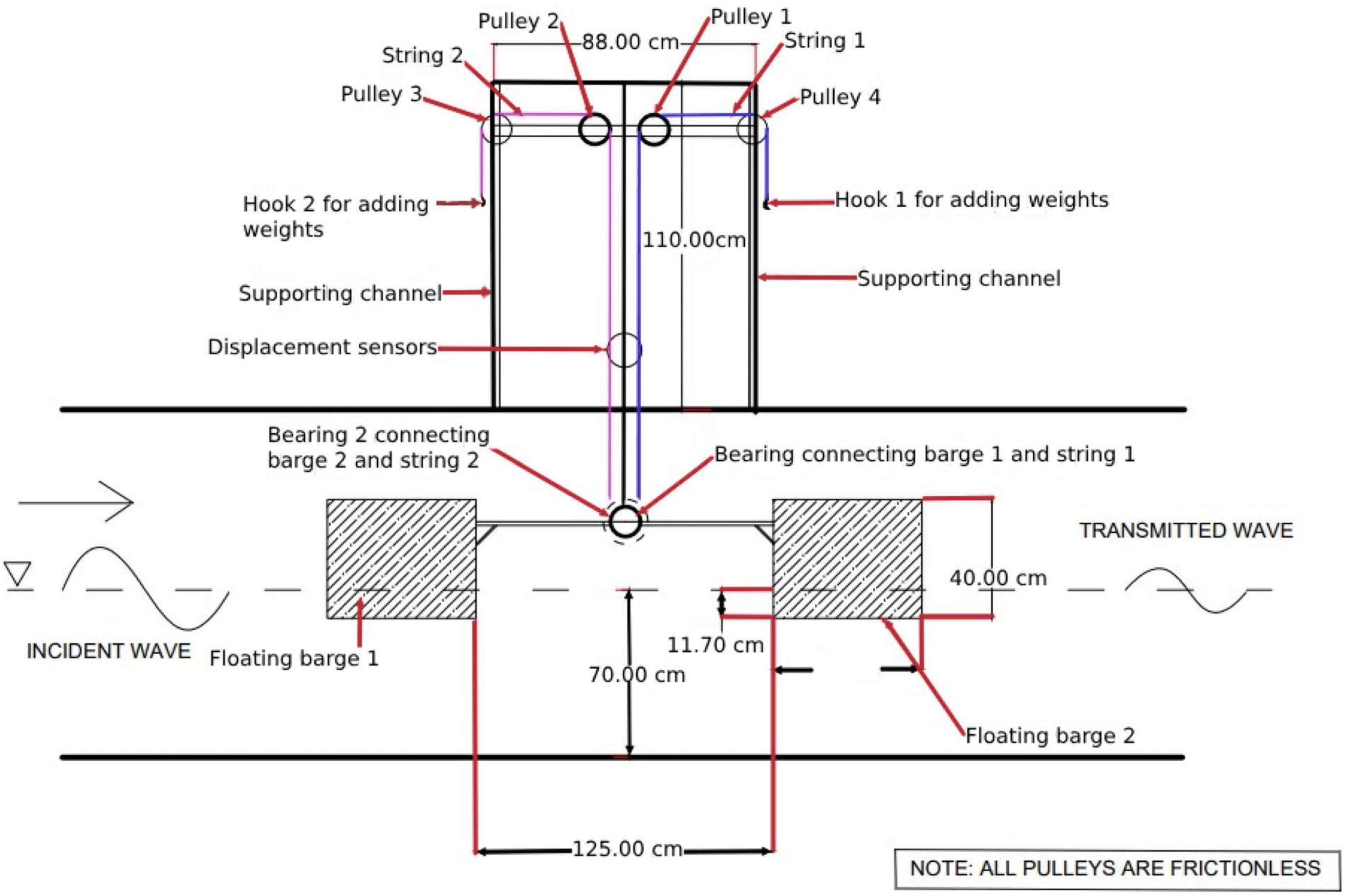

Fig. 1. Side view of the twin floating barge with the connection arrangements.

energy dissipation characteristics for a wide range of wave and PTO conditions.

The subsequent section discusses the methodology, including model fabrication, experimental investigation, and data analysis. The “Results and Discussion” section is followed by “Conclusions, Limitations, and Future Work” section.

Methodology

This section presents the methodology with details of the model, simulation of the PTO system, instrumentation and calibration, experimental setup, hydrodynamic input conditions, and data analysis.

The floating WEC considered in this study consists of two pontoons with a center-to-center spacing of 1.75 m. These twin-floating pontoons or rafts are hinged to a fixed shaft. This constrains the movement to only one degree of freedom, namely, swinging on the hinge attached to the fixed horizontal shaft. The power output was estimated by simulating a mechanical PTO system that provides suitable damping forces for the swinging raft. The mechanical power output was obtained by measuring the torque of the swinging pontoons in conjunction with the angular velocity of the raft on the shaft. Experiments were performed with the following measurements for each random wave:

1. Incident wave height measured in the absence of the model to avoid reflection from the model and accurately estimate the input conditions;
2. The model’s wave field at the seaside to assess wave reflection characteristics;
3. Wave fields at the lee side to assess wave transmission characteristics;
4. Torque generated by a known resisting force over the swinging pontoons on a fixed shaft; and
5. The angular velocity of the swinging raft.

The selected model was scaled to 1:10 based on a thorough analysis of the capabilities of the wave maker and wave flume size. This is a concept validation study, and a narrow wave flume was selected to circumvent the complexities of wave diffraction and nonlinear interactions by ensuring that the wave–structure interactions were limited to the direction of wave propagation. The flume width was 0.60 m, and the model was designed with a width of 0.58 m, leaving a gap of 0.01 m on both sides to mitigate the risk of the model colliding with the glass wall during wave action. A flexible rubber material was fixed to prevent the leakage of wave energy through these gaps. The floating barge was constructed with acrylic sheets with a thickness of 12 mm. The barge has a length of 0.50 m along the wave direction, a width of 0.58 m, and a depth of 0.40 m. The connection details of the barge are depicted in Fig. 1.

Fig. 2 provides a close-up view of the rigidly fixed stainless-steel shaft (diameter = 0.10 m). The rod from the raft was attached to a frictionless bearing with a diameter of 0.22 m, allowing it to oscillate along with the raft. Fig. 3 illustrates how the model was secured to the flume.

The PTO simulation setup for a single raft is shown in Fig. 4. As shown, the stainless steel wire connecting the bearing and resisting weight passes through frictionless pulleys. A force sensor with a

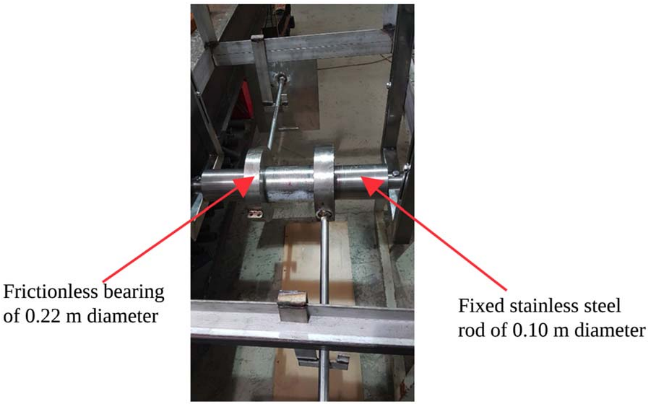

Fig. 2. Rod connecting the swinging arrangement of a raft.

Fig. 3. Arrangement used to fasten the model to the wave flume.

capacity of 1,000 N was attached to the stainless steel wire. This setup allowed measurements of the forces generated in the wire during oscillations when a known resisting weight was added at the end of the wire. A thread from the bearing passes through a potentiometer (as shown in Fig. 4) parallel to the steel wire to measure its displacement. The resisting weight emulated the damping of the PTO system from 0 to 20 kg (in 2 kg increments) and from 20 to 25 kg (in 5 kg increments). This was adopted to indicate the variation in the resisting force for raft oscillation. Table 1 lists the complete dimensional details of the model and other parameters for simulating the damping characteristics of the PTO system.

The natural period of oscillation and nondimensional damping of the pontoon were assessed for all different PTO damping weights. The natural period of oscillation varied from 1.113 to 1.15 s for the range of resisting weights. The nondimensional damping coefficient κ was estimated using the following equation:

$$\kappa = \frac{1}{2\pi} \ln \left\{ \frac{z_1 - z_2}{z_3 - z_4} \right\} \tag{1}$$

where z_1 = first positive peak of the displacement time series; z_2 = first negative peak; z_3 = second positive peak; and z_4 = subsequent negative peak. Typically, as the resisting load increases, the damping coefficient (κ) should also increase owing to the damping caused by the added weights. The lowest value of κ was 0.272 for the resisting weight of 0.1 kg (minimum resistance to the oscillation), and the maximum value was 0.357 when the resisting weight was 25 kg.

Hydrodynamic tests were conducted in the glass wave flume facility at the Coastal and Hydraulic Laboratory of the Kuwait Institute of Scientific Research at the Shuwaikh campus, Kuwait. The flume dimensions were 54.5 (length) × 1.2 (height) × 0.6 m (width). The wave generation system consisted of a piston-type wave maker with active wave absorption control. Five conductive-type wave probes manufactured by Danish Hydraulic Institute

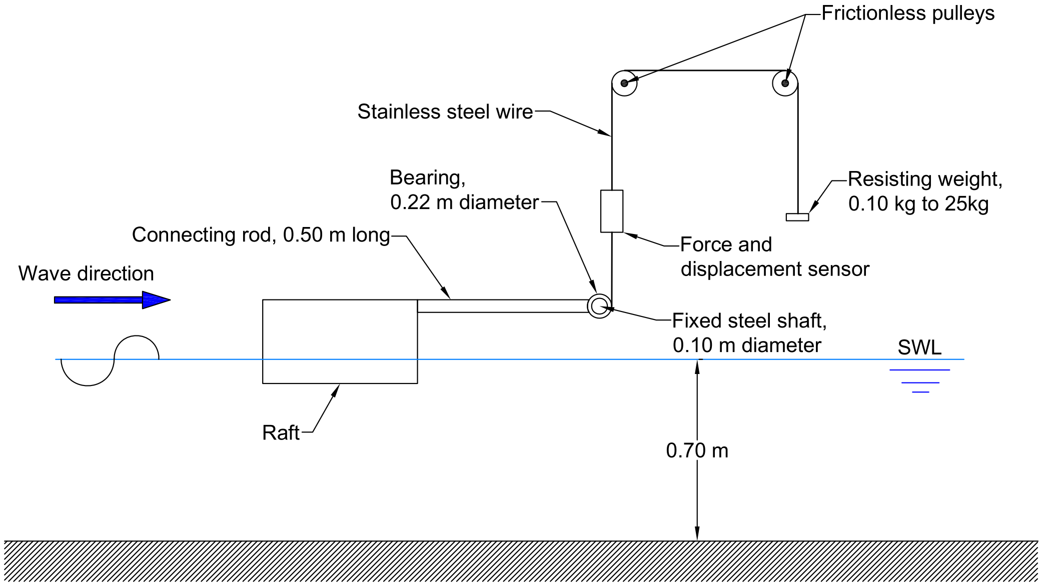

Fig. 4. PTO system arrangement (shown using a single-raft model for clarity).

Table 1. Dimensional details of the model and other essential parameters used to simulate the damping behavior of the PTO system

Parameters	Dimensions (or) measures	Unit	Material and comments
Raft size	0.58 (width, w) × 0.40 (height, h) × 0.50 (length, l in the direction of wave propagation)	m × m × m	Acrylic sheet
Center-to-center distance between the rafts (B)	1.75	m	—
Average total weight of each raft	35.47	kg	—
Effective lever arm of the center of gravity of each raft from the center of the fixed shaft	0.829	m	Estimated by considering the weights of three steel plates attached to the acrylic box and the steel rod connecting the raft and fixed shaft
Average moment owing to the raft weight on the center of the fixed shaft	288.40	N·m	—
Average draft of the raft (initial draft without load on the PTO simulating wire)	0.11	m	The draft varied as the weight on the wire increased from 100 g to 25 kg
Water depths used (d)	0.70	m	—
PTO resisting weights added	0.1, 2, 4, 6, 8, 10, 12, 14, 16, 18, 20, and 25	kg	—
Lever arm of resisting weight	0.13	m	—
Moments resisting the raft oscillation for $d = 0.70$ m	0.12, 2.55, 5.10, 7.65, 10.20, 15.30, 17.85, 20.40, 22.95, 25.50 and 31.87	N·m	—
Moment ratio M (average moment owing to the raft weight on the center of the fixed shaft/moments resisting the raft oscillation for $d = 0.70$ m)	2,262.3, 113.1, 56.6, 37.7, 28.3, 22.6, 18.9, 16.2, 14.1, 12.6, 11.3 and 9.0	—	As the value of M increases, the damping of the PTO system decreases

(DHI) were used to measure the wave surface elevations at different locations, as shown in Fig. 5. The wave probes had a range of 600 mm with a resolution of 0.15 mm and an accuracy of 2% of maximum. The displacement sensors, also from DHI, were used for measuring the motion of the rafts. It had a maximum range of 122 mm and could detect displacements of at least 0.025 mm. The two DHI force sensors capable of measuring loads up to 1,000 N with a resolution of 0.25 N were also used. All the instruments were connected to the DHI data acquisition system. All sensors were calibrated every week to ensure constancy and quality of the collected data. All calibrations had linear regression coefficients higher than 0.993. The wave maker was highly capable of generating the same wave conditions repeatedly. In addition, the variations in the calibration coefficients of all sensors during the experiments were minimal. Thus, the error of these experiments was assumed to be very small. A detailed error analysis was not performed as the study was only a preliminary concept validation.

An ideal hybrid WEC should provide minimum wave transmission and maximum power conversion efficiencies across a broad range of input conditions. This can be achieved to a certain extent by minimizing wave reflection and dissipation and ensuring that the floating wave-energy device can resonate for a range of wave periods. This is one of the long-term objectives of this study. The resulting knowledge is likely to aid in the development of cost-effective commercial wave-energy utilization with competitive investments and returns. This study primarily focuses on finding the effects of wave height and period on wave transmission, reflection, dissipation, and mechanical power conversion. In addition, the effect of change in PTO damping on these parameters will also be investigated.

Experimental Test Matrix

All the random waves considered in the study were generated based on the JONSWAP spectrum. The input parameters considered for this study are incident significant wave height (H_s), peak wave period, T_p, water depth (d), width of the raft (W), center-to-center distance between the floating raft models (B), and wavelength (L_p). Herein, the incident wavelength (L_p) is estimated using the dispersion relation:

$$L_p = 1.56.T_p^2 \tanh(2\pi d/L_p) \tag{2}$$

The input parameters can be converted to the following nondimensional terms:

1. Relative wave height, H_s/d;
2. Incident wave steepness, H_s/L_p;

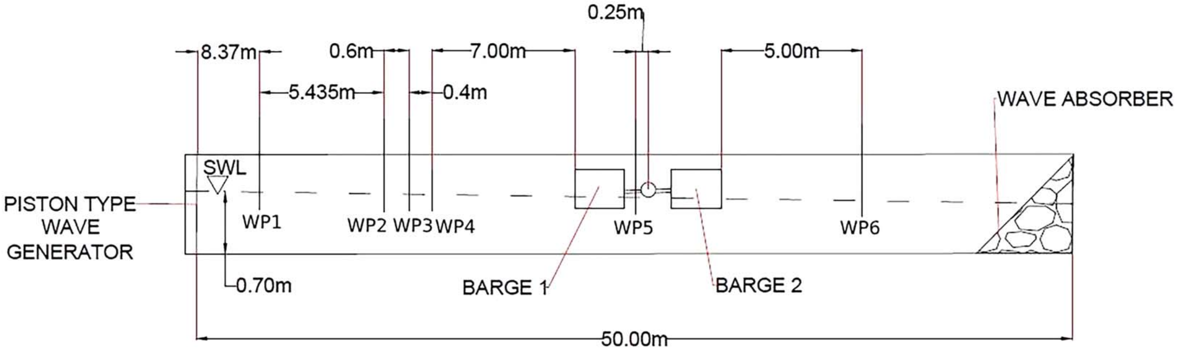

Fig. 5. Wave probe arrangement.

Table 2. Selection of peak wave periods to be generated based on the selected L_p/B values

L_p/B required	Corresponding wavelength, L_p (m)	d/L_p	d/L_o	Required peak wave period, T_p (s)
0.50	0.875	0.800	0.800	0.749
1.00	1.750	0.400	0.395	1.066
2.00	3.500	0.200	0.170	1.625
3.00	5.250	0.133	0.091	2.221
4.00	7.000	0.100	0.056	2.838

3. Relative water depth, d/L_p;
4. Relative wavelength, L_p/B or B/L_p; and
5. Ursell parameter, $U_r(U_r = H_s L_p^2/d^3)$.

The depth for this study was 0.7 m. The wavelengths were selected such that the relative wavelength (L_p/B) could be varied from 0.5 to 4 (as shown in Table 2). This provided an understanding of the performance of the model at different relative positions of the wave crest and trough with respect to the center of the floating rafts.

Five wave periods were considered for the random wave study, and in each period, three wave heights ($H_s = 0.05$, 0.10, and 0.15 m) were examined. However, because of the maximum speed and displacement limitations of the piston-type wave maker, it was not possible to generate $H_s = 0.15$ m for $T_p = 0.749$ and 2.838 s. As a result, 13 random wave conditions were assessed. All runs were executed with a sample rate of 40 Hz, which was adequate for capturing all the peak values for this study.

The significant wave heights $H_s = 0.05$, 0.10, and 0.15 m correspond to relative wave height ratios of 0.071, 0.142, and 0.214, respectively. Table 3 provides the details of the normalized input parameters for a water depth (d) of 0.70 m. The relative water depth d/L_p ranged from 0.1 to 0.8, indicating that the results of this study apply to intermediate- and deep-water conditions. The wave steepness (H_s/L_p) (ranging from 0.008 to 0.083) indicates that the incident wave condition covers mild to steep conditions. The Ursell parameter (ranging from 0.095 to 18.049) implies that the study encompasses linear and nonlinear conditions. Hence, the results of the present study are valid for a wide range of real-world conditions.

Data Analysis

The incident wave data were measured using Wave probes WP1, WP2, WP3, and WP4 in the absence of the model in the flume. The wave probe arrangement used in this experiment is shown in Fig. 5. Linear spectral analysis was performed using software program MIKEZERO (version 2012) to obtain the zeroth moment m_o, which was used to calculate the significant wave height using the following relationship:

$$H_s = 4\sqrt{(m_0)} \tag{3}$$

The average of the wave heights from the first four wave probes was used as incident wave heights. Wave transmission coefficient (K_t), wave reflection coefficient (K_r), wave-energy dissipation coefficient (K_l), and mechanical power absorbed by each raft device were estimated as discussed in the following.

The transmitted wave surface elevation was measured using Wave probe 6, which was maintained 7 m behind the model. The significant wave height of the transmitted waves, H_{ts}, was determined by linear spectral analysis, as mentioned in the previous section. The coefficient of transmission, K_t, was estimated by estimating the ratio of the transmitted wave height to the incident wave height.

Data from WP2, WP3, and WP4 were used to estimate the reflected wave height and coefficient of reflection, K_r (the ratio of reflected wave height to incident wave height). The reflection analysis software program MIKEZERO is based on the method described by Mansard and Funke (1980) and improved by Zelt and Skjelbreia (1992). The distance between WP2 and WP3 was 0.60 m, and that between WP2 and WP4 was 0.100 m. The distances between the reflection wave probes were used as inputs for the reflection analysis. Three wave probes were used rather than two to prevent singularity problems during the reflection analysis.

The average incident wave power (P_{inc} in W) for a random wave field with significant wave height (H_s) and peak period (T_p) over the width (B) is given by

$$P_{\text{inc ave}} = [0.55\, H_s^2 T_p B]1{,}000 \tag{4}$$

where H_s and B are in meters and T_p is in seconds. The assessed incident wave powers in random waves for different incident wave conditions at a water depth of 0.70 m are listed in Table 4. For the selected wave conditions, the range of incident wave power is from 0.45 to 27.06 W.

Table 3. Normalized input parameters for a water depth $d = 0.70$ m

Run number	Peak wave period, T_p (s)	Intended significant wave height, H_s (m)	Wavelength, L_p (m)	B/L_p	d/L_p	Measured significant incident wave height (m)	Measured incident wave steepness, H_s/L_p	Ursell parameter ($H_s L_p^2/d^3$)
1	0.749	0.05	0.875	2.00	0.8	0.043	0.049	0.095
2	0.749	0.10	0.875	2.00	0.8	0.068	0.077	0.151
3	1.066	0.05	1.750	1.00	0.4	0.063	0.036	0.566
4	1.066	0.10	1.750	1.00	0.4	0.117	0.067	1.048
5	1.066	0.15	1.750	1.00	0.4	0.145	0.083	1.298
6	1.625	0.05	3.500	0.50	0.2	0.068	0.019	2.429
7	1.625	0.10	3.500	0.50	0.2	0.141	0.040	5.040
8	1.625	0.15	3.500	0.50	0.2	0.199	0.057	7.102
9	2.221	0.05	5.250	0.33	0.13	0.065	0.012	5.217
10	2.221	0.10	5.250	0.33	0.13	0.140	0.027	11.278
11	2.221	0.15	5.250	0.33	0.13	0.192	0.037	15.441
12	2.838	0.05	7.000	0.25	0.1	0.059	0.008	8.381
13	2.838	0.10	7.000	0.25	0.1	0.126	0.018	18.049
Minimum	0.749	0.05	0.875	0.25	0.1	0.043	0.008	0.095
Maximum	2.838	0.15	7.0	2.0	0.8	0.192	0.083	18.049

Table 4. Average incident wave power for different combinations of (H_s,T_p)

Peak wave period, T_p (s)	Generated incident wave height, H_s (m)	P_{inc} (W)
0.749	0.043	0.450
0.749	0.068	1.134
1.066	0.063	1.414
1.066	0.117	4.844
1.066	0.145	7.431
1.625	0.068	2.481
1.625	0.141	10.679
1.625	0.199	21.208
2.221	0.065	3.089
2.221	0.140	14.437
2.221	0.192	27.064
2.838	0.059	3.223
2.838	0.126	14.950

The mechanical power [P_{abs} (t)] (in W) at an instant (t) for the swinging shaft can be obtained by the following equation:

$$P_{\text{abs}}(t) = \text{Torque} \times \text{Angular velocity} \tag{5}$$

Here, torque is in Newton meters and angular velocity in radians per second. Fig. 4 shows that the applied load is transmitted as force F to the shaft, which oscillates with the wave action on the rafts. Thus, the torque acting on the shaft with a radius of r at time t can be calculated as follows:

$$\text{Torque at time } (t) = F(t) \cdot r \tag{6}$$

Notably, the shaft undergoes only a small oscillation $\Delta\theta$ within a marginal variation in time Δt (as shown in Fig. 6). Thus, the oscillation (in radians) can be estimated from the vertical displacement ΔD using the following relationship:

$$\Delta\theta = \frac{\Delta D}{r} \tag{7}$$

Hence, the angular velocity can be expressed as follows:

$$\text{Angular velocity} = \Delta D(t)/(r \cdot \Delta t) \tag{8}$$

Therefore, the power equation [Eq. (5)] can be rewritten as follows:

$$\begin{aligned} P_{\text{abs}}\ (t) &= (F(t) \cdot r)\left(\frac{\Delta D(t)}{(r \cdot \Delta t)}\right) \\ &= \left(F(t)\left(\frac{\Delta D(t)}{\Delta t}\right)\right) \end{aligned} \tag{9}$$

The force and displacement on the wire varied with the oscillation of the raft in response to the wave action. Hence, the energy or power of the wire can be assessed for the total duration of data collection, and the average power can be assessed to estimate the mechanical power conversion efficiency.

Examples of the measured force and displacement time series of a wire connected to a seaside raft are provided in Figs. 7(a and b), respectively. The case shown here involves a regular wave (for better representation) with a wave height of 0.15 m, a period of 2.532 s, and an applied force of 98 N on the wires. The force on the wire exceeded 98 N when the raft was under the influence of a wave crest and was <98 N under the influence of a wave trough. This occurred owing to the acceleration and deceleration of the wire during raft oscillation. The assessed mechanical power time series under identical conditions is shown in Fig. 7(c). Regular wave time series are shown here only for ease of representation, as they are shorter and can easily represent the power estimation calculations. The same method was applied to the irregular wave time series to calculate mechanical power.

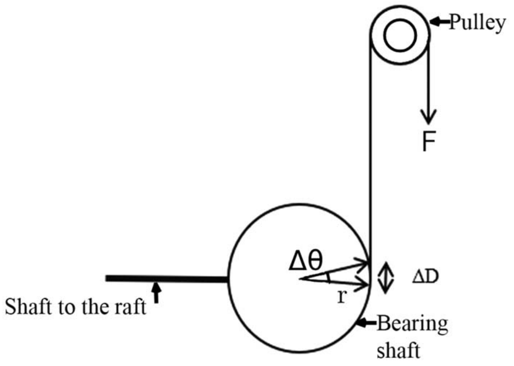

Fig. 6. Power assessment for an oscillating shaft.

Mechanical power conversion efficiency was defined as the ratio of the average mechanical power to the average incident wave power. It was calculated as follows:

$$\eta = \frac{(P_{\text{abs}})_{\text{ave}}}{(P_{\text{inc}})_{\text{ave}}} \tag{10}$$

The mechanical power conversion efficiencies for Raft 1 (the seaside raft) and Raft 2 (the rear-side raft) are indicated by η_1 and η_2, respectively.

The wave transmission coefficient, K_t, reflection coefficient, K_r, and mechanical power conversion efficiencies for Raft 1 (the seaside raft) and Raft 2 (the rear-side raft) (η_1 and η_2, respectively) were estimated, as discussed in the previous sections. From the law of energy conservation, the dissipation coefficient K_l can be assessed using the following equation:

$$K_l = (1 - K_t^2 - K_r^2\ )^{1/2} \tag{11}$$

However, in this case, the incident wave energy was also converted into mechanical power. Therefore, the dissipation coefficient includes the power conversion efficiency of the rafts as well as the actual loss owing to turbulence, shear friction, and wave breaking. The dissipation coefficients can be divided into power efficiencies, and the actual dissipation can be rewritten as follows:

$$K_{l\ \text{actual}} = (1 - K_t^2 - K_r^2 - \eta_1 - \eta_2)^{1/2} \tag{12}$$

These parameters were influenced by the input wave conditions, model dimensions, and PTO conditions. The relationship between the variable terms and the output parameter can be expressed by the following nondimensional equation:

$$(K_t, K_r, K_l, K_{l\ \text{actual}}) = f\ \left(\frac{d}{L_p} \text{or} \frac{B}{L_p} \text{or} \frac{L_p}{B} \text{or} \frac{l}{L_p}, \frac{H_s}{d}, \frac{H_s}{L_p}, M\right) \tag{13}$$

where the moment ratio (M) is the ratio of the moment of the raft by its weight to the moment of the weight added to the wire. The moment of the raft was calculated by the product of the weight of the raft and the distance between the center of the fixed shaft and the center of the raft, which was equal to 288.41 N·m. The counter moment is the added weight multiplied by the lever arm (which is the radius of the bearing). The values of M are listed in Table 1. As the relative depth (d/L_p) is an important parameter used in the selection of a suitable location for the installation of WEC devices, it is preferred to discuss the results related to this term. Therefore, Eq. (13)

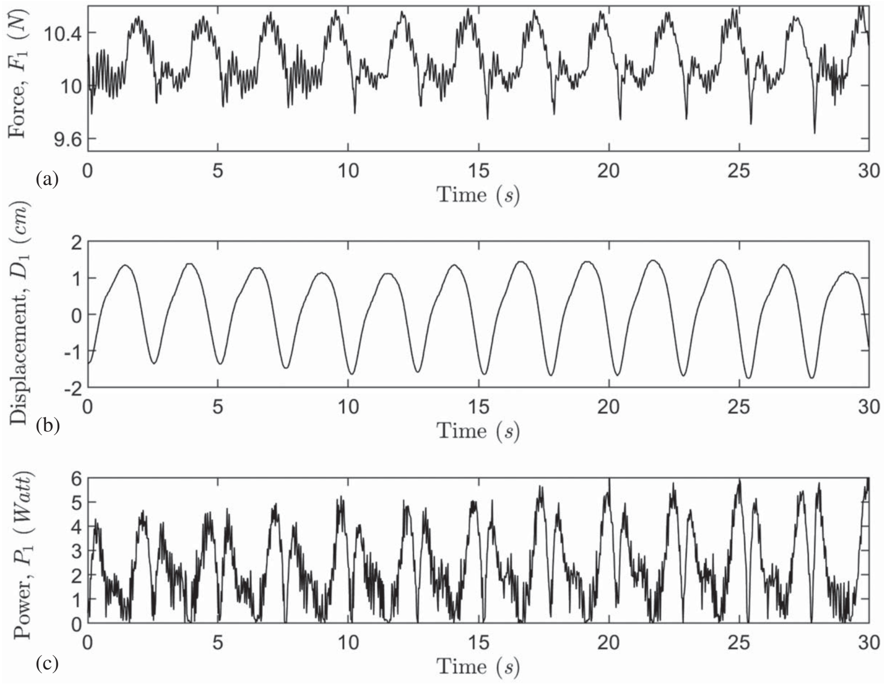

Fig. 7. (a) Force time series; (b) displacement time series; and (c) mechanical power time series for the wire attached to Raft 1 when a PTO load of 98 N is placed on the wire (all the time series apply for $H_i = 0.15$ m and $T = 2.532$ s).

can be rewritten as follows:

$$(K_t, K_r, K_l, K_{l\,\text{actual}}) = f\left(\frac{d}{L_p}, \frac{H_s}{d}, \frac{H_s}{L_p}, M\right) \tag{14}$$

Similarly, the mechanical power conversion efficiency can be expressed as a function of the wave, structure, and PTO damping parameters as follows:

$$(\eta_1, \eta_2) = f\left(\frac{d}{L_p}, \frac{H_s}{d}, \frac{H_s}{L_p}, M\right) \tag{15}$$

Notably, the water depth ($d = 0.70$ m), distance between the rafts (B), and length along the direction of wave propagation (l) were constant throughout the study. Therefore, the relative depth also represents the structural parameters according to the following equation:

$$\frac{d}{L_p} = 0.4\left(\frac{B}{L_p}\right) = 1.4\left(\frac{l}{L_p}\right) \tag{16}$$

Results and Discussion

Effects of Incident Wave Height and Peak Wave Period on K_t, K_r, K_l, η_1, and η_2

The results for low, medium, and high PTO damping values are discussed for a better understanding of the effect of varying the PTO damping on the hydrodynamic performance of the device.

K_t, K_r, K_l, η_1, and η_2 during Low/Minimum PTO Damping

Fig. 8 is a typical plot of K_t, K_r, K_l, η_1, and η_2 with a force of 0.98 N on the PTO wires [the corresponding moment ratio (M) is 2,262.3]. This is the minimum PTO damping because the force on the wire was significantly smaller compared with the weight of the raft. The figures are plotted with relative wavelength (L_p/B) on the x-axis to indicate the effects of the peak wave period. The center-to-center distance between the rafts (B) remained constant throughout the study; therefore, the change in L_p/B reflects the change in wavelength, which is proportional to the peak wave period. L_p/B ranged from 0.5 to 4.0. The variations in the significant wave heights were represented by different H_s/d ratios with values of 0.071, 0.142, and 0.214.

Fig. 8(a) shows the change in wave transmission with the peak period. The peak transmission occurs when the relative wavelength (L_p/B) is equal to 4. When $L_p/B = 0.5$ (the corresponding d/L_p value is 0.8, which corresponds to a deep-water condition), the transmission approaches zero. In the case of $L_p/B = 1$ (the corresponding d/L_p was 0.4, which corresponds to a near-deep-water condition), K_t is in the range of 0.23–0.37. Long waves transmit more energy from the still water level (SWL) to the seabed because of their high energy density. Short waves transmit less wave energy because the incident wave energy dies abruptly from the SWL toward the seabed. The energy near the SWL effectively interacts with the outer surface of the raft, resulting in the dynamic responses of the rafts (swinging on the shaft), the radiation of waves on both sides of the model, and reflection and dissipation. Fig. 8(a) shows that as Lp/B increases, the wave transmission increases; however, the change is not consistent with the significant wave height increase. Conversely, the wave reflection varied consistently [Fig. 8(b)]. From an engineering perspective, this trend is good because if K_r is reduced in high-energy incident wave cases, the remaining wave energy (incident wave energy minus reflected wave energy), which is relatively high for larger incident wave heights, will be available for energy conversion. For a relative wavelength greater than two, the reflection coefficient was <0.34. Fig. 8(c) shows that an increase in L_p/B typically causes a reduction in dissipation. However, no clear variational trend in K_l was observed with an increase in the incident wave height. This shows that the dissipation mostly depends on the position of the wave peaks with respect to the raft rather than the wave height. For instance, more dissipation occurs when both rafts are in phase. If

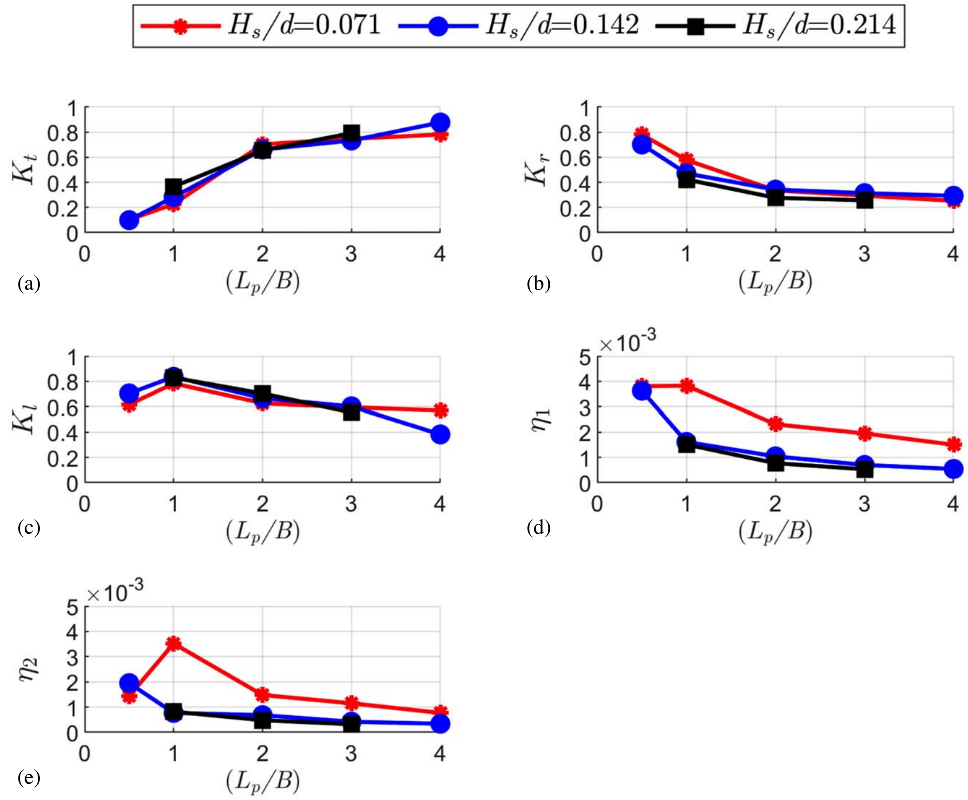

Fig. 8. Effects of wave height and peak wave period on (a) wave transmission; (b) wave reflection; (c) wave-energy dissipation; (d) power conversion efficiency of the seaside raft; and (e) power conversion efficiency of rear side raft (all the plots are for $d = 0.70$ m and a damping load of 0.98 N.

they are in antiphase, the interactions of waves with the raft are less prominent, thus causing less prominent dissipation effects.

The values of the mechanical power conversion efficiency [shown in Figs. 8(d and e)] are small because there is almost no damping condition as the force on the wire was minimal. However, the power conversion efficiency decreases as the wave period and wave height increase.

K_t, K_r, K_l, η_1, and η_2 during Moderate PTO Damping

The hydrodynamic characteristics and mechanical power conversion for identical wave height and peak wave period conditions (as those used in Fig. 8 figures), albeit with a 14 kg load on the wire (moment ratio = 16.2), were plotted to analyze the effect of moderate PTO damping. Fig. 9 shows the efficiencies η_1 and η_2 for this moderate damping, while the reflection, dissipation, and transmission follow the same trends as those in low PTO cases; therefore, these outcomes are not shown here. When the PTO damping was increased, the resistance in the motion of the rafts increased; this altered the hydrodynamic behavior.

With regard to the power conversion efficiencies, η_1 was maximized when the incident wave was mild; correspondingly, it was reduced when the wave height increased. Hence, the proposed WEC is more effective during mild incident wave conditions, which are more probable in open oceans. The peak value of efficiency occurred at $L_p/B = 1.0$, with 0.6 for the seaside raft and 0.48 for the rear-side raft. Herein, the incident peak wave period was 1.066 s, which is also within the range of the natural period of oscillation of the rafts (which is between 1.113 and 1.15 s). This verifies that designing the rafts with a natural period of oscillation closer to the most predominant peak wave period at the selected location maximizes the power production by resonance. However, for $L_p/B = 1.0$, the sum of seaside raft efficiency and rear side raft will be greater than one. This is not acceptable for the energy conversion relationship mentioned in Eq. (12), showing that the PTO is overdamping for this specific wave condition. The PTO load is exerting more energy on the raft than the incident waves. This can be explained in terms of energy; as the incident wave periods are closer to the natural period of oscillation, the raft will be displaced more owing to resonance. This raises the

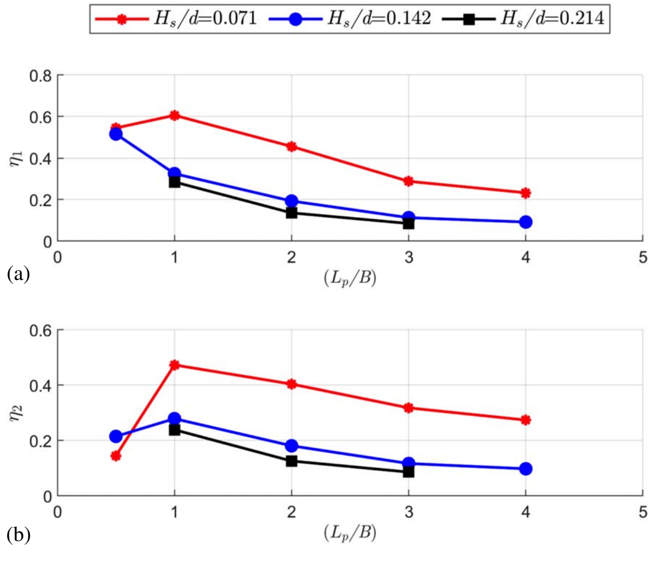

Fig. 9. Effects of wave height and peak wave period on the power conversion efficiencies of the (a) seaside raft; and (b) rear-side raft (plots for $d = 0.70$ m and wire load of 137.2 N).

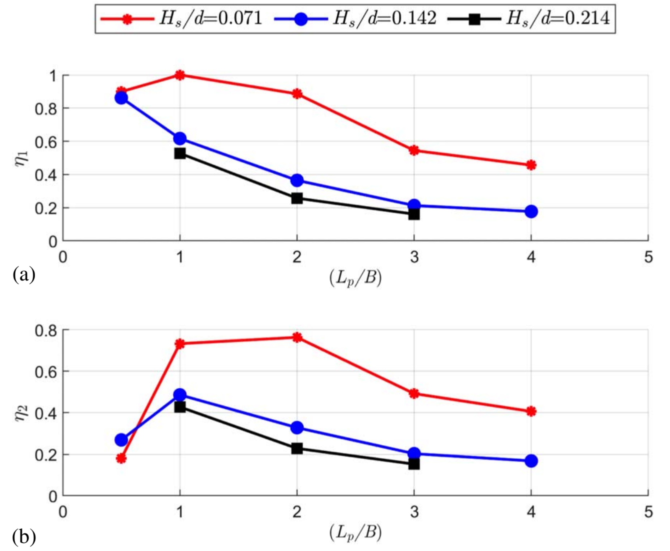

Fig. 10. Effects of wave height and peak wave period on power conversion efficiency of the (a) seaside raft; and (b) the rear-side raft (both the plots are for $d = 0.70$ m and a damping load of 245 N).

hanging weights relatively more when the wave crest acts on the raft than the heights attained in other wave conditions, thus increasing the potential energy of the applied weights. This (stored) higher potential energy will be converted to kinetic energy as the wave crest recedes from the raft, pushing the raft back to the water.

K_t, K_r, K_l, η_1, and η_2 during High PTO Damping

The maximum weight applied to the model for damping was 25 kg. This corresponded to a moment ratio of 9.0. The observed trends in K_t, K_r, and K_l for the wave height and peak wave periods were similar to those in previous conditions. This indicates that PTO damping does not have a significant influence on the reflection, transmission, and dissipation coefficients. The mechanical power conversion efficiency varied significantly for both sea- and rear-side rafts, as shown in Fig. 10. For the seaside raft [Fig. 10(a)], the peak value of the efficiency is almost one at a low-wave height condition ($H_s/d = 0.071$). According to the law of energy conservation, this is not feasible, showing that this situation is an example of high overdamping where the individual efficiency itself becomes more than one. Furthermore, for the low-height condition ($H_s/d = 0.071$) and the lower periods of the moderate condition, the sum of the efficiencies was greater than one as force is exerted by the damping system rather than by incoming waves. This indicates that the case in which the damping is 245 N represents an overdamping situation in which the energy conservation relationship [Eq. (12)] cannot be satisfied and should be avoided.

Effects of Incident Wave Steepness on K_t, K_r, K_l, η_1, and η_2

To demonstrate the effect of wave steepness on K_t, K_r, K_l, η_1, and η_2, two PTO damping parameters were considered, namely, 39.2 and 196 N. Fig. 11 shows the plots of K_t, K_r, and K_l for 39.2 N of damping. The measured incident significant wave heights differed marginally from the intended incident significant wave heights. The measured wave steepness was used to plot the results. However, the legend provides the intended significant wave heights.

Fig. 11(a) shows that when the wave steepness increases, the wave transmission decreases. The slope of the reduction is steeper for smaller incident waves ($H_s = 0.05$ m) and more gradual for higher incident wave conditions ($H_s = 0.10$ and 0.15 m). This plot shows that for any wave steepness, a range of transmission coefficient (K_t) exists that indicates nonlinear behavior. For example, for H_s/L_p from 0.036 to 0.04, the K_t values of 0.26 and 0.71, respectively, correspond to waves that have smaller and larger wavelengths. K_t reduces as the wave steepness increases at a constant incident wave height. Notably, the broad ranges of K_t and H_s/L_p are caused by the variations in the wave height and wavelength.

The effect of wave steepness on the reflection coefficient is illustrated in Fig. 11(b). As the incident wave becomes steeper, the reflection coefficient increases. When the steepness is low, more wave energy is transmitted, resulting in less reflection. Conversely, a steeper wave tends to dissipate more energy [as shown in Fig. 11(c)], leading to the transmission of a smaller proportion of energy. Steeper waves tend to dissipate energy by breaking at the raft and creating significant turbulence around the floating body region.

The influence of incident wave steepness on the mechanical power conversion efficiency of the raft system is shown in Fig. 12. The mechanical power conversion efficiency of the seaside raft increases as a function of the incident wave steepness. The efficiency of the rear side raft increases up to a certain point and then decreases. This abrupt reduction in efficiency for the rear-side raft occurs because the seaside raft prevents the wave energy from passing under its keel. The efficiency was high when the incident wave heights were marginal (thick circles) and decreased as the significant wave height increased (thin circles and squares). For example, when the wave steepness (H_s/L_p) varied from 0.036 to 0.04, the efficiency of the seaside raft was 0.18 for a mildly significant wave height of 0.05 m. When the significant wave height was 0.10 m and the wavelength was varied accordingly to obtain the same H_s/L_p, the efficiency was reduced to 0.11. When the significant wave height was 0.15 m and with the same H_s/L_p (the wavelength was increased further), the efficiency of the seaside raft dropped to 0.037. Thus, efficiency increased when the wave height was constant, while the wave period was reduced. Notably, for any H_s/L_p value, the combined effect of both H_s and L_p influences the efficiency over a broad range. Waves with short periods have more efficiency as they are closer to the natural period of oscillation of the raft. In contrast, the power conversion efficiency decreases significantly when the peak wave period increases at a constant wave steepness. Furthermore, the power conversion by the seaside raft is typically better than that at the rear-side raft, particularly for steeper waves. This could be because the incident wave energy interacting with the seaside raft is larger than that interacting with the rear-side raft, owing to the significant dissipation and prevention of the transmission of short-length waves. At a particular wave height, both rafts are equally efficient for power conversion when the wave steepness is moderate. This can be because the dissipation was moderate and the transmission was sufficient to ensure that both rafts received an equal amount of incident wave power at mild wave steepness values.

Similar plots are provided for a PTO load of 196 N (Figs. 13 and 14) to demonstrate the importance of increasing the PTO damping for K_t, K_r, K_l, η_1, and η_2. Varying the PTO load had less impact on the wave transmission coefficient. Similar observations were made for the reflection and dissipation coefficients. In the case of efficiency, the overall trends were similar to those associated with lower damping levels. The main difference was in the magnitude of power conversion efficiency, which was higher.

Effects of PTO Damping on K_t, K_r, K_l, η_1, and η_2

The discussion of the results in this section starts with low-incident wave energy ($H_s/d = 0.071$). It is followed by discussing the

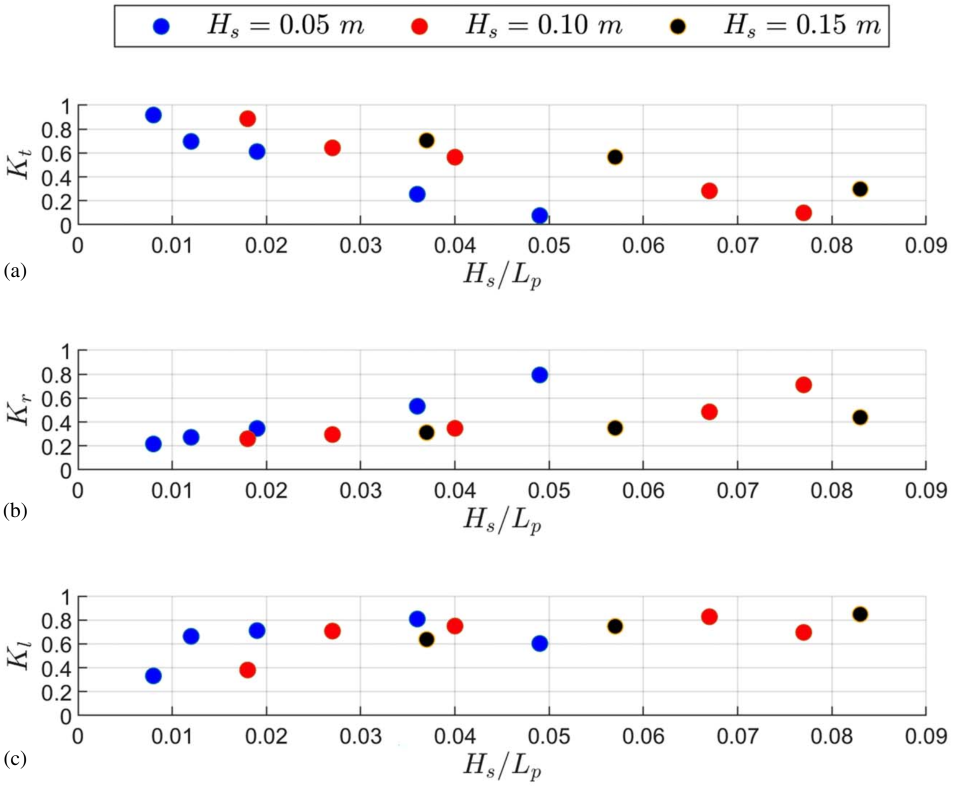

Fig. 11. K_t, K_r, and K_l for a water depth of 0.70 m and for PTO damping corresponding to 39.2 N. Effects of incident wave steepness, H_s/L_p on (a) K_t; (b) K_r; and (c) K_l.

medium-wave energy ($H_s/d = 0.142$) and high-wave energy ($H_s/d = 0.214$) conditions.

Effects of PTO Damping on K_t, K_r, K_l, η_1, and η_2 for Waves of Low-Input Wave-Energy Conditions ($H_s/d = 0.071$)

Fig. 15 shows the effects of varying PTO damping on K_t, K_r, K_l, η_1, and η_2 at a low-input wave-energy condition ($H_s/d = 0.071$). The insights from these plots can be used to design floating wave-energy systems for Kuwait, countries around the Arabian Gulf, and locations with similar wave conditions. The change in PTO damping is represented by the moment ratio M. It was observed that varying M had only a marginal effect on the wave transmission. These marginal variations occur primarily in long wave cases (at smaller d/L_p values), owing to the dynamic response of the pontoons and successive wave generation on the lee side. However, for small d/L_p values ($d/L_p < 0.2$), the variation in K_t with respect to that in M did not display a clear trend. The K_t value was determined to be >0.6 when $d/L_p < 0.2$. K_t values <0.2 were achieved only when $d/L_p > 0.4$. The lowest K_t values (0.05–0.1) were observed only when $d/L_p = 0.8$.

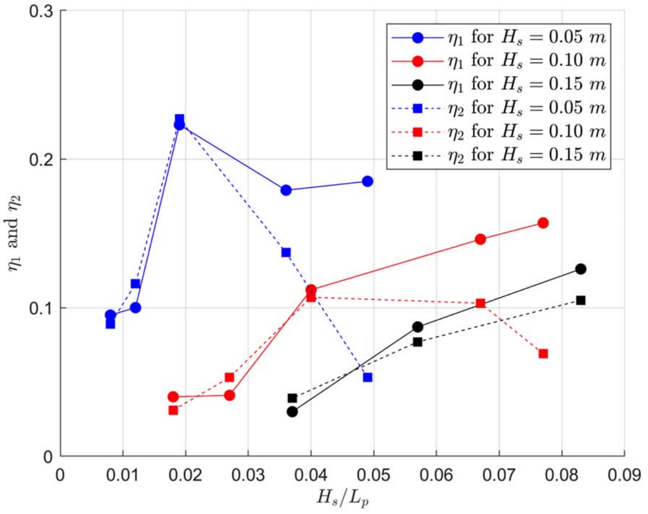

Fig. 12. Effects of incident wave steepness, H_s/L_p, on η_1 and η_2 for a water depth of 0.70 m and for PTO damping corresponding to 39.2 N.

Fig. 15(b) shows the reflection coefficient under identical input conditions. Varying M did not affect reflection for the range of relative depths studied. The peak value of K_r was 0.8 and occurred at a relative depth equal to 0.8. Fig. 15(c) shows the effects of damping on dissipation. It is shown that varying M influences K_l, particularly at low d/L_p values. The peak value of dissipation occurs at $d/L_p = 0.4$. For the range of PTO damping studied, the dissipation varied from 25% to 75%.

The mechanical power conversion efficiency, η_1, of the seaside raft is shown in Fig. 15(d). It was observed that varying M caused a significant variation in η_1. This variation was higher near the natural period of the oscillation of the raft (which was an average of 1.13 s for the range of PTO damping and the corresponding $d/L_p = 0.36$). For the highest damping applied in the present study, η_1 was close to one, and the sum of η_1 and η_2 was greater than one. This situation should be avoided, as it does not satisfy the energy conservation relation mentioned in Eq. (12). The peak efficiency occurred when $d/L_p = 0.4$, which is closer to the natural period of oscillation of the raft. It is necessary to define the effective frequency range for liberal hydrodynamic performance conditions as the range of wave frequency for which $K_t < 0.5$ and $\eta_1 > 0.2$

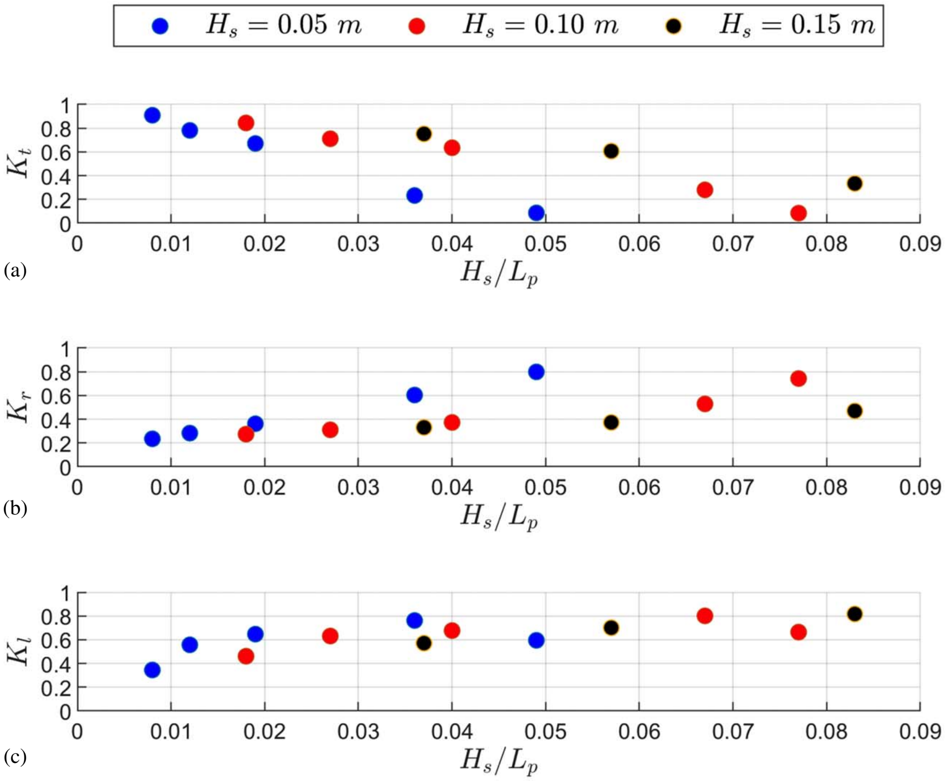

Fig. 13. K_t, K_r, and K_l for a water depth of 0.70 m and for PTO damping corresponding to 196 N. Effects of incident wave steepness, H_s/L_p, on (a) K_t; (b) K_r; and (c) K_l.

[as reported in Ning et al. (2017) for a dual pontoon WEC-type breakwater] to assess its cumulative hydrodynamic performance. Liberal hydrodynamic performance was observed as d/L_p varied from 0.267 to 0.8. The PTO damping to achieve $\eta_1 > 0.2$ is $M < 37.7$, which corresponds to 39.2 N. For more stringent hydrodynamic performance conditions ($K_t < 0.2$ and $\eta_1 > 0.4$), the effective frequency range for optimum damping in terms of d/L_p is 0.4–0.8. The system damping for PTO to achieve efficiency >40% requires damping levels >78.4 N. Hence, the WEC can be used effectively for a broad range of wave periods and PTO damping conditions to achieve the effective frequency range for liberal ($K_t < 0.5$ and $\eta_1 > 0.2$) and stringent ($K_t < 0.2$ and $\eta_1 > 0.4$) hydrodynamic performance.

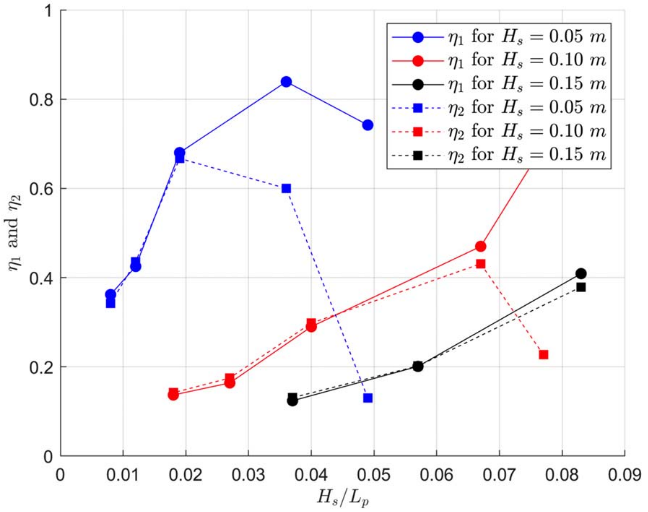

Fig. 14. Effects of incident wave steepness H_s/L_p on η_1 and η_2 for a water depth of 0.70 m and for PTO damping corresponding to 196 N.

Fig. 15(e) shows the mechanical power conversion efficiency η_2 of the rear side raft for $H_s/d = 0.071$. For liberal hydrodynamic performance ($K_t < 0.5$ and $\eta_2 > 0.2$), the range of effective frequency in terms of d/L_p was 0.267–0.77. The system's damping for PTO to achieve ≥20% of mechanical power conversion efficiency was $M < 28.3$. For stringent hydrodynamic performance ($K_t < 0.2$ and $\eta_2 > 0.4$), the effective frequency range in terms of d/L_p was 0.4–0.65. The system damping for PTO to achieve ≥40% mechanical conversion efficiency was $M < 16.2$. For $d/L_p = 0.8$, the mechanical power conversion efficiency (for all the damping conditions) was <0.2. This is because the seaside raft permits only long waves to be transmitted and act on the rear-side raft. Hence, if the field condition is closer to $d/L_p = 0.8$, twin-floating barriers are not required.

Effects of PTO Damping on K_t, K_r, K_l, η_1, and η_2 for Moderate-Input Wave-Energy Conditions ($H_s/d = 0.142$)

Like the low-input wave-energy conditions, no clear trend was observed in the variation in K_t with the variation in M or damping. As observed under low-wave conditions, $K_t < 0.2$ is feasible only for $d/L_p > 0.5$ under medium-wave conditions. K_t attained the lowest value of 0.1 when $d/L_p = 0.8$. Furthermore, varying M had an insignificant effect on K_r for long waves ($d/L_p < 0.2$). However, it was primarily for short waves ($d/L_p = 0.4$–0.8). The peak value of the reflection ($K_r = 0.7$) occurred at $d/L_p = 0.8$. Similarly, the peak value of dissipation occurred at $d/L_p = 0.4$.

Fig. 16(a) shows the mechanical power conversion efficiency, η_1, for $H_s/d = 0.142$. For the liberal hydrodynamic performance condition ($K_t < 0.5$ and $\eta_1 > 0.2$), the effective frequency range in terms of d/L_p varied from 0.267 to 0.8. The required system damping for PTO to achieve ≥20% mechanical power conversion

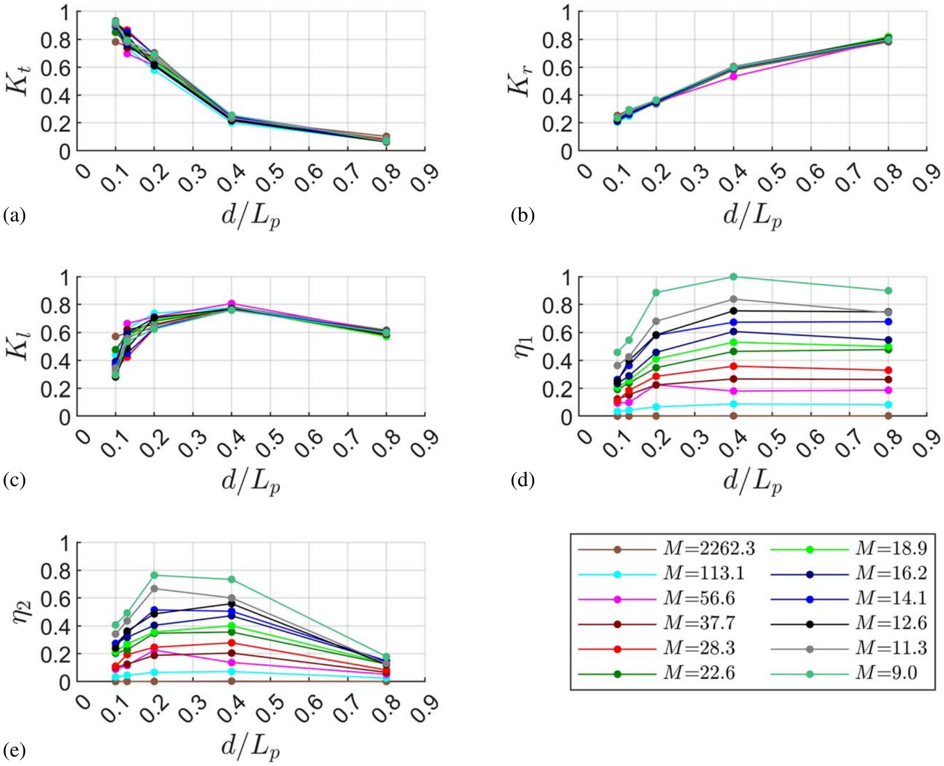

Fig. 15. Effects on (a) K_t; (b) K_r; (c) K_l; (d) power conversion efficiency of the seaside raft (η_1); and (e) power conversion efficiency of the rear-side raft (η_2) by varying the damping [all the plots are for a water depth of 0.70 m and for $H_s/d = 0.071$ (low-input wave-energy condition)].

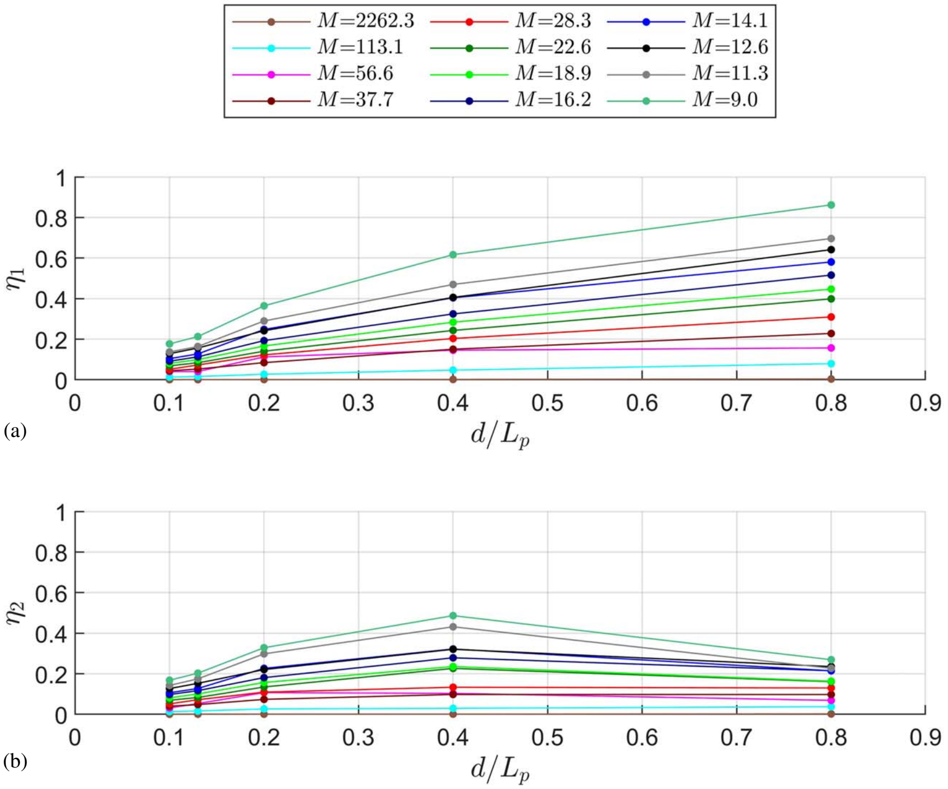

Fig. 16. Effects on (a) power conversion efficiency of the seaside raft (η_1); and (b) power conversion efficiency of the rear-side raft (η_2) by varying the damping for a water depth of 0.70 m and for $H_s/d = 0.142$ (moderate input wave-energy condition).

efficiency was $M < 37.7$. This is similar to the previous case with a low incident significant wave height. For the stringent hydrodynamic performance condition ($K_t < 0.2$ and $\eta_1 > 0.4$), the effective frequency range for optimal damping was available for $d/L_p > 0.56$. For $d/L_p = 0.8$, the mechanical conversion efficiency increased consistently with an increase in damping and attained a value of 0.86 for $M = 9$.

Fig. 16(b) illustrates the mechanical power conversion efficiency, η_2, of the rear-side raft. This was less than the efficiency values for lower wave heights. Hence, it can be stated that an increase in the significant wave height reduced the peak mechanical power conversion efficiency of the rear-side raft. For the liberal hydrodynamic performance condition ($K_t < 0.5$ and $\eta_2 > 0.2$), the effective frequency range with optimum damping ($M = 9$ for this case) in terms of d/L_p varied from 0.267 to 0.8. The system damping for PTO to achieve ≥20% mechanical power conversion efficiency was $M < 22.6$. For the stringent performance condition ($K_t < 0.2$ and $\eta_2 > 0.4$), no effective frequency range was available. This was because the highest efficiency achieved was <0.4. For $d/L_p = 0.8$ (the condition when the seaside raft achieved the maximum efficiency), the mechanical power conversion efficiency for the rear-side raft increased when damping levels increased. However, the maximum value was 0.27.

Effects of PTO Damping on K_t, K_r, K_l, η_1, and η_2 for High Wave-Energy Conditions ($H_s/d = 0.214$)

Varying M had a negligible effect on K_t, even for short waves. K_t was higher than 0.7 and increased to 0.85 for $d/L_p = 0.13$. $K_t < 0.2$ is infeasible for the range of d/L_p studied for this high wave-energy input condition. The peak value of reflection occurred at $d/L_p = 0.4$. Similarly, varying M had an insignificant effect on K_r.

As observed in the case of low and moderate wave-energy conditions, varying M influences K_l. The peak value of dissipation occurred at $d/L_p = 0.4$ because of the steepening of waves, breaking on the raft, high-intensity vortex shedding, and shear friction over the floating body. Varying M from 9 to 2,262.3 resulted in an observable variation in K_l, particularly in the low-frequency region [Fig. 17(a)]. Recall that random waves with a significant wave height of 0.15 m could not be generated in cases where the d/Lp values were equal to 0.1 and 0.8. Therefore, fewer data points than those for the previous plots are available here.

Fig. 17(b) shows the mechanical power conversion efficiency η_1 of the seaside raft for identical input conditions. The maximum value of seaside raft efficiency was 0.53 for the highest damping condition. This is significantly lower than the efficiency value for low- and moderate-input wave-energy conditions discussed previously. For the liberal hydrodynamic performance conditions ($K_t < 0.5$ and $\eta_1 > 0.2$), the effective frequency range for optimum damping in terms of d/L_p varied from 0.3 to 0.4. The system damping level to ensure that the PTO achieved ≥20% higher mechanical power conversion efficiency was $M < 22.6$. No effective wave period range was found to attain the stringent hydrodynamic performance conditions ($K_t < 0.2$ and $\eta_1 > 0.4$). This was because the $K_t < 0.2$ condition was not achieved for the range of studied d/L_p values.

Regarding the mechanical power conversion of the rear side raft, for $M = 9$, the peak value of η_2 was 0.43. This is less than the efficiency values for lower wave heights. This verified that an increase in the significant wave height reduced the mechanical power conversion efficiency of the rear-side raft [Fig. 17(c)]. For the liberal hydrodynamic performance ($K_t < 0.5$ and $\eta_2 > 0.2$) and for optimum damping in the present study ($M = 9$), the effective frequency range was $d/L_p > 0.3$. As stated in the case of the seaside raft, no wave period range was available to adhere to the stringent hydrodynamic performance conditions ($K_t < 0.2$ and $\eta_1 > 0.4$), although the highest efficiency achieved was 0.43 because $K_t < 0.2$ was not achieved.

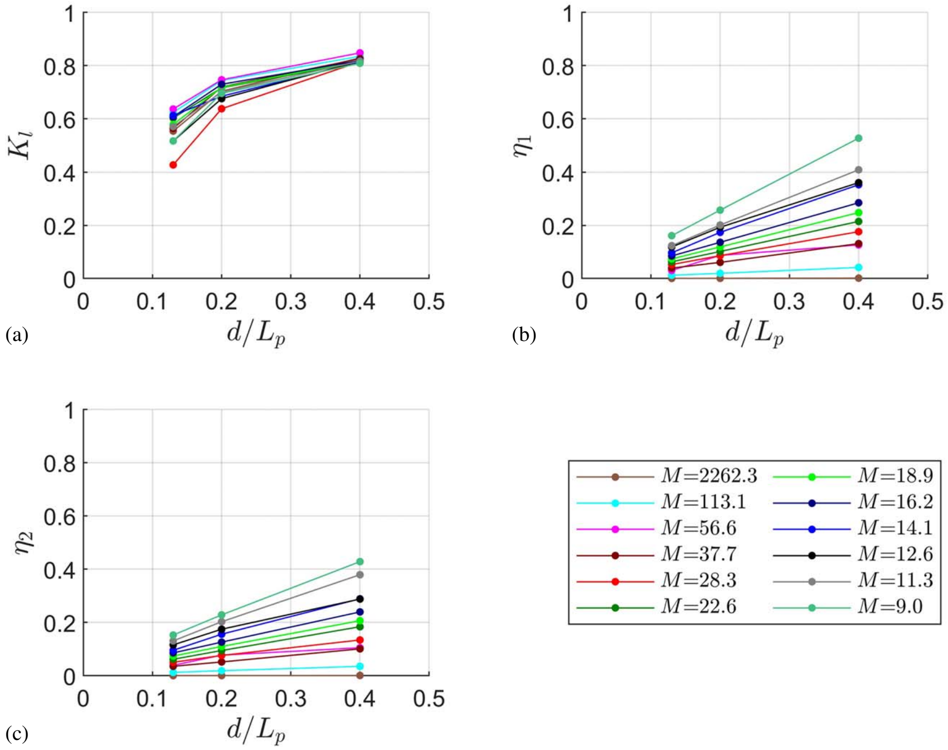

Fig. 17. Effects on (a) K_l; (b) power conversion efficiency of the seaside raft (η_1); and (c) power conversion efficiency of the rear-side raft (η_2) by varying the damping for $H_s/d = 0.214$ (high-input wave-energy condition).

Notably, at higher damping levels, the sum of the efficiency of the sea- and rear-side rafts was greater than one. This does not satisfy the energy conservation relation [Eq. (12)], and lower damping is recommended for such wave conditions. PTO damping of 78.4 N or a moment ratio of 28.3 was found to be the most optimal, as this condition satisfied the energy conversion for all the tested wave conditions. Peak efficiencies of 0.35 for the seaside raft and 0.27 for the rear-side raft were achieved with this optimal damping.

Conclusions, Limitations, and Future Work

In this study, the wave transmission, reflection, dissipation, and mechanical power conversion efficiencies of a twin-raft floating wave-energy device were experimentally investigated under wide ranges of random wave conditions and simulated PTO damping conditions. It is important to select the correct damping because excessive damping can provide high resistance to the hinged motion and thereby reduce efficiency, whereas excessively small damping can cause unbounded motion of the floats, which cannot be converted effectively to mechanical power. For the current results, the physical parameters of the device were maintained constant, such as the center-to-center distance between the rafts (1.75 m), water depth, and mean draft of the rafts without PTO damping load. The conclusions of this study are as follows:

1. The hydrodynamic coefficients, such as those of reflection, dissipation, and transmission, were highly sensitive to changes in the peak wave period. Even though the significant wave height affected the hydrodynamic performance, no consistent variation was observed. This shows that the wave period is the most important parameter in selecting a suitable location for such devices.
2. For low water depth or shallow water areas, the PTO damping or resistance to the motion of floating bodies highly influences the wave transmission, reflection, and dissipation, particularly at low values of the relative water depth (d/L_p).
3. Overdamping situations were noticed, especially for lower wavelengths in which the sum of the efficiency values is greater than one or when the energy conservation relationship is not satisfied. Such damping conditions should be avoided in those wave conditions.
4. The optimum PTO damping for the studied condition was 78.4 N, or a moment ratio of 28.3; the energy conservation relationship was satisfied for all the studied wave conditions, and peak efficiencies of 0.35 and 0.27 for the sea- and rear-side rafts, respectively, were achieved.
5. The ranges of wave transmission values and conversion efficiencies were discussed for liberal and stringent hydrodynamic performance. Accordingly, this device is suitable as a hybrid WEC as it can effectively convert wave energy and wave breakers.

The conclusions of this study can help further develop the concept of a WEC that can be used as a hybrid device. The results of this study were obtained under liberal and stringent hydrodynamic performance conditions to assess the effective range of available frequencies to satisfy the conditions that can aid the design and use of other devices similar to this concept. Additional research is required to apply this concept on a larger scale. The experiments were performed in a narrow wave flume with a width marginally larger than that of the device to confine the wave propagation to one direction of the device and minimize the nonlinear wave–structure interaction. This is not the case in actual sea conditions. Therefore, additional studies are required to understand the performance of the device in wave basins. Owing to time constraints, only one model was tested herein. However, the geometry of the device (e.g., the dimensions and shape of the raft) is an important parameter that can influence performance. Therefore, these factors should be investigated in future studies. The shape of the raft is cuboidal with sharp edges. This can cause viscous drag. Thus, the performance can be improved further by using a curved body, as demonstrated by Stansby et al. (2015).

Data Availability Statement

Some or all data, models, or codes that support the findings of this study are available from the corresponding author upon reasonable request.

Acknowledgments

The authors gratefully acknowledge the partial sponsorship (Project Code: PR18-15EV-05) by the Kuwait Foundation for Advancement of Sciences (KFAS) for pursuing this research. The Kuwait Institute for Scientific Research (KISR) provided the wave flume and instruments. The authors acknowledge the support of the Coastal Management Program secretaries, Mr. J. Ashok and Mr. Khalid Atala.

References

Barstow, S., G. Mork, D. Mollison, and J. Cruz. 2008. “The wave energy resource.” In *Ocean wave energy*, edited by J. Cruz, 93–132. Berlin: Springer.

Cabral, T., D. Clemente, P. Rosa-Santos, F. Taveira-Pinto, T. Morais, F. Belga, and H. Cestaro. 2020. “Performance assessment of a hybrid wave energy converter integrated into a harbor breakwater.” *Energies* 13 (1): 236. https://doi.org/10.3390/en13010236.

Cheng, Y., L. Fu, S. Dai, M. Collu, C. Ji, Z. Yuan, and A. Incecik. 2022. “Experimental and numerical investigation of WEC-type floating breakwaters: A single-pontoon oscillating buoy and a dual-pontoon oscillating water column.” *Coastal Eng.* 177: 104188. https://doi.org/10.1016/j.coastaleng.2022.104188.

Clément, A., et al. 2002. “Wave energy in Europe: Current status and perspectives.” *Renewable Sustainable Energy Rev.* 6 (5): 405–431. https://doi.org/10.1016/S1364-0321(02)00009-6.

Falnes, J. 2007. “A review of wave-energy extraction.” *Mar. Struct.* 20: 185–201. https://doi.org/10.1016/j.marstruc.2007.09.001.

He, F., and Z. Huang. 2014. “Hydrodynamic performance of pile-supported OWC-type structures as breakwaters: An experimental study.” *Ocean Eng.* 88: 618–626. https://doi.org/10.1016/j.oceaneng.2014.04.023.

He, F., Z. Huang, and A. W. K. Law. 2012. “Hydrodynamic performance of a rectangular floating breakwater with and without pneumatic chambers: An experimental study.” *Ocean Eng.* 51: 16–27. https://doi.org/10.1016/j.oceaneng.2012.05.008.

He, F., J. Leng, and X. Zhao. 2017. “An experimental investigation into the wave power extraction of a floating box-type breakwater with dual pneumatic chambers.” *Appl. Ocean Res.* 67: 21–30. https://doi.org/10.1016/j.apor.2017.06.009.

Howe, D., J.-R. Nader, and G. Macfarlane. 2020. “Experimental investigation of multiple Oscillating Water Column Wave Energy Converters integrated in a floating breakwater: Energy extraction performance.” *Appl. Ocean Res.* 97: 102086. https://doi.org/10.1016/j.apor.2020.102086.

Ilyas, A., S. A. R. Kashif, M. A. Saqib, and M. M. Asad. 2014. “Wave electrical energy systems: Implementation, challenges and environmental issues.” *Renewable Sustainable Energy Rev.* 40: 260–268. https://doi.org/10.1016/j.rser.2014.07.085.

Li, D., S. Sharma, A. G. L. Borthwick, H. Huang, X. Dong, Y. Li, and H. Shi. 2023. "Experimental study of a floating two-body wave energy converter." *Renewable Energy* 218: 119351. https://doi.org/10.1016/j.renene.2023.119351.

Mansard, E. P. D., and E. R. Funke. 1980. "The measurement of incident and reflected spectra using a least squares method." *Coastal Eng. Proc.* 1 (17): 8. https://doi.org/10.9753/icce.v17.8.

Martinelli, L., P. Ruol, and C. Favaretto. 2016. "Hybrid structure combining a wave energy converter and a floating breakwater." In *Proc., 26th Int. Ocean and Polar Engineering Conf.* Rhodes, Greece: International Society of Offshore and Polar Engineers (ISOPE).

Masuda, Y. 1986. "An experience of wave power generator through tests and improvement." In *Hydrodynamics of ocean wave-energy utilization*, edited by D. V. Evans, and A. F. O. de Falcão, 445–452. Berlin, Germany: Springer.

McCormick, M. E. 1981. *Ocean wave energy conversion*. North Chelmsford, MA: Courier Corporation.

Mørk, G., S. Barstow, A. Kabuth, and M. T. Pontes. 2010. "Assessing the global wave energy potential." In Vol. 3 of *Proc., 29th Int. Conf. on Ocean, Offshore, and Arctic Engineering*, 447–454. New York: ASME.

Ning, D., X. Zhao, M. Göteman, and H. Kang. 2016. "Hydrodynamic performance of a pile-restrained WEC-type floating breakwater: An experimental study." *Renewable Energy* 95: 531–541. https://doi.org/10.1016/j.renene.2016.04.057.

Ning, D., X. Zhao, L. Chen, and M. Zhao. 2018. "Hydrodynamic performance of an array of wave energy converters integrated with a pontoon-type breakwater." *Energies* 11 (3): 685. https://doi.org/10.3390/en11030685.

Ning, D.-Z., X.-L. Zhao, M. Zhao, M. Hann, and H.-G. Kang. 2017. "Analytical investigation of hydrodynamic performance of a dual pontoon WEC-type breakwater." *Appl. Ocean Res.* 65: 102–111. https://doi.org/10.1016/j.apor.2017.03.012.

Pelc, R., and R. M. Fujita. 2002. "Renewable energy from the ocean." *Marine Policy* 26: 471–479. https://doi.org/10.1016/S0308-597X(02)00045-3.

Peng, W., Y. Zhang, X. Yang, J. Zhang, R. He, Y. Liu, and R. Chen. 2020. "Hydrodynamic performance of a hybrid system combining a fixed breakwater and a wave energy converter: An experimental study." *Energies* 13 (21): 5740. https://doi.org/10.3390/en13215740.

Peng, W., Y. Zhang, Q. Zou, X. Yang, Y. Liu, and J. Zhang. 2021. "Experimental investigation of a triple pontoon wave energy converter and breakwater hybrid system." *IET Renewable Power Gener.* 15 (14): 3151–3164. https://doi.org/10.1049/rpg2.12214.

Ransley, E. J., D. M. Greaves, A. Raby, D. Simmonds, M. M. Jakobsen, and M. Kramer. 2017. "RANS-VOF modelling of the Wavestar point absorber." *Renewable Energy* 109: 49–65. https://doi.org/10.1016/j.renene.2017.02.079.

Rosa-Santos, P., F. Taveira-Pinto, M. López, and C. A. Rodríguez. 2022. "Hybrid systems for marine energy harvesting." *J. Mar. Sci. Eng.* 10 (5): 633. https://doi.org/10.3390/jmse10050633.

Shahabi-Nejad, M., and A. H. Nikseresht. 2022. "A comprehensive investigation of a hybrid wave energy converter including oscillating water column and horizontal floating cylinder." *Energy* 243: 122763. https://doi.org/10.1016/j.energy.2021.122763.

Stansby, P., E. C. Moreno, and T. Stallard. 2015. "Capture width of the three-float multi-mode multi-resonance broadband wave energy line absorber M4 from laboratory studies with irregular waves of different spectral shape and directional spread." *J. Ocean Eng. Mar. Energy* 1: 287–298. https://doi.org/10.1007/s40722-015-0022-6.

Yang, I., T. Tahsin, and A. Incecik. 2023. "Numerical investigations of a pivoted point absorber wave energy converter integrated with breakwater using CFD." *Ocean Eng.* 274: 114025. https://doi.org/10.1016/j.oceaneng.2023.114025.

Zelt, J. A., and J. E. Skjelbreia. 1992. "Estimating incident and reflected wave fields using an arbitrary number of wave gauges." *Coastal Eng.* 1992: 777–789.

Zhang, H., X. Ding, B. Zhou, L. Zhang, and Z. Yuan. 2019. "Hydrodynamic performance study of wave energy–type floating breakwaters." *J. Mar. Sci. Appl.* 18 (1): 64–71. https://doi.org/10.1007/s11804-019-00064-y.

Zhang, Y., X. Chen, P. Xu, X. Zhao, O. el Moctar, and C. Jiang. 2023. "Performance of a raft-type wave energy converter with diverse mooring configurations." *J. Mar. Sci. Eng.* 11: 2352. https://doi.org/10.3390/jmse11122352.

Zhao, X. L., D. Z. Ning, Q. P. Zou, D. S. Qiao, and S. Q. Cai. 2019. "Hybrid floating breakwater-WEC system: A review." *Ocean Eng.* 186: 106126. https://doi.org/10.1016/j.oceaneng.2019.106126.

Zheng, S., and Y. Zhang. 2018. "Analytical study on wave power extraction from a hybrid wave energy converter." *Ocean Eng.* 165: 252–263. https://doi.org/10.1016/j.oceaneng.2018.07.021.